





Casimir-Lifshitz force between graphene-based structures out of thermal equilibriumYoussef Jeyar ^{1,*}, Kevin Austry,¹ Minggang Luo ¹, Brahim Guizal ¹, H. B. Chan,^{2,3,4} and Mauro Antezza ^{1,5,†}¹Laboratoire Charles Coulomb (L2C), UMR 5221 CNRS-University of Montpellier, F-34095 Montpellier, France²Department of Physics, The Hong Kong University of Science and Technology, Clear Water Bay, Kowloon, Hong Kong, China³William Mong Institute of Nano Science and Technology, The Hong Kong University of Science and Technology, Clear Water Bay, Kowloon, Hong Kong, China⁴Center for Metamaterial Research, The Hong Kong University of Science and Technology, Clear Water Bay, Kowloon, Hong Kong, China⁵Institut Universitaire de France, 1 rue Descartes, Paris Cedex 05, F-75231, France

(Received 30 May 2023; revised 24 August 2023; accepted 28 August 2023; published 7 September 2023; corrected 27 September 2023)

We study the nonequilibrium Casimir-Lifshitz force between graphene-based parallel structures held at different temperatures and in the presence of an external thermal bath at a third temperature. The graphene conductivity, which is itself a function of temperature, as well as of chemical potential, allows us to tune *in situ* the Casimir-Lifshitz force. We explore different nonequilibrium configurations while considering different values of the graphene chemical potential. Particularly interesting cases are investigated, where the force can change sign going from attractive to repulsive or where the force becomes nonmonotonic with respect to chemical-potential variations, contrary to the behavior under thermal equilibrium.

DOI: [10.1103/PhysRevB.108.115412](https://doi.org/10.1103/PhysRevB.108.115412)**I. INTRODUCTION**

van der Waals dispersion forces occur between polarizable objects and are a quantum, relativistic, and macroscopic physical manifestation of both quantum and thermal fluctuations of the electromagnetic field. Generally, these forces increase rapidly as the separation between the objects decreases, becoming dominant over other forces at the micron scale and below. As a result, they could play an important role in nano- and micro-electromechanical systems. If the whole system is at thermal equilibrium, these forces are described by the Lifshitz, Dzyaloshinskii, and Pitaevskii theory [1,2] which, in the middle of the 1950s, considerably generalized the Casimir ideal-reflectors configuration [3]. This allowed us to account for objects made by real materials and consider finite temperature, opening the possibility to study a large number of new experimental realizations. We hence name this general van der Waals interaction the Casimir-Lifshitz (CL) force. Fifty years later, that theory has been further generalized to systems out of thermal equilibrium (OTE) where the different objects are held at different temperatures and are immersed in a thermal environmental bath held at a third temperature, with the full system being in a stationary OTE state. The new nonequilibrium theory was first developed for atom-surface configurations [4–7], showing rich and unexpected behavior (change of sign of the force which can possibly become a repulsive, different temperature and separation distance power law, ...). Some of these predictions were verified in experiments with ultracold atoms trapped close to a hot substrate [8,9]. Internal atomic nonequilibrium features have been also investigated [10,11]. This theory was subsequently generalized to macroscopic planar objects [4,12] and finally to (two

or more) objects of arbitrary shape and dielectric function [13–16], opening new opportunities in the study of the CL interaction in the general and richer framework of nonequilibrium systems. A single closed-form expression based on scattering matrix theory has been derived [14,16] accounting for both CL force out of equilibrium and the concurrent radiative heat transfer [17] occurring between the objects, hence unifying the momentum and energy transfer in those systems. Afterwards, expressions have been derived also using the Green's function formalism [18,19].

With this general OTE theory at hand, the CL force OTE has been intensively explored for different geometric configurations (atom surface [5,8,14,16], parallel planes [12,14,16], diffraction gratings [20]). In addition to geometric features, the CL force is also very sensitive to the material dielectric properties. It is hence interesting to study the effects that emerging materials can bring to the features of CL force OTE. One of the most interesting materials today is graphene, due to its peculiar properties [21,22], like, for instance, the possibility to tune, *in situ*, its Fermi energy (or chemical potential μ) and hence its electric conductivity by a simple applied voltage, and the presence of thermally activated surface modes exalting the thermal CL force at very short separations [23–25]. By using the explicit atom-surface expression derived in Ref. [14], the atom-graphene force has been recently investigated [26] for $\mu = 0$. In this paper we investigate the CL force OTE between two graphene-based parallel structures (see scheme on Fig. 1) made by suspended graphene or SiO₂ slabs coated with graphene, in different thermal nonequilibrium configurations involving three different temperatures, and also for different values of chemical potential μ .

In Sec. II we describe the physical systems, the dielectric properties of the involved materials and the general model and formalism. In Sec. III we present and analyze the numerical calculations of the force in different configurations.

*youssef.jeyar@umontpellier.fr

†mauro.antezza@umontpellier.fr

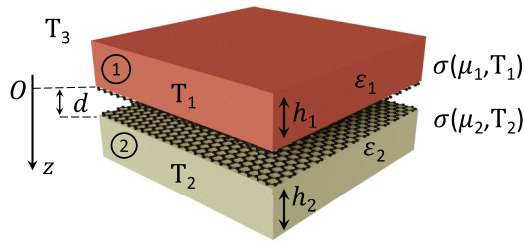


FIG. 1. Sketch of the system under consideration, consisting of two parallel graphene-based structures 1 and 2 held at temperatures T_1 and T_2 , respectively, in the presence of an environmental bath at temperature T_3 . The two graphene sheets have conductivity $\sigma_1(\omega, \mu_1, T_1)$ and $\sigma_2(\omega, \mu_2, T_2)$, depending on their chemical potential μ_i and temperature T_i .

II. PHYSICAL SYSTEM AND MODEL

The physical system under consideration is depicted in Fig. 1. It consists of two dielectric slabs of thicknesses h_1 and h_2 and relative dielectric permittivities $\epsilon_1(\omega)$ and $\epsilon_2(\omega)$ that are facing each other and separated with distance d . They are covered with graphene sheets having conductivities $\sigma_1(\omega, \mu_1, T_1)$ and $\sigma_2(\omega, \mu_2, T_2)$ respectively where μ_1 (μ_2) is the chemical potential of graphene sheet 1 (graphene sheet 2) and T_1 (T_2) is the temperature of graphene covered slab 1 (graphene covered slab 2). T_3 is the temperature of the environment. We emphasize that the environmental temperature is not the temperature of the electromagnetic field. Instead, it is just the temperature of the walls surrounding the two bodies.

A. Casimir-Lifshitz pressure

The Casimir-Lifshitz pressure (CLP) out of thermal equilibrium between two parallel homogeneous dielectric slabs of

finite thicknesses, covered with graphene sheets, separated by a distance d and acting on body 1 can be expressed as [12]

$$P_{1z}(T_1, T_2, T_3) = \frac{P_z^{(eq)}(T_1) + P_z^{(eq)}(T_2)}{2} + \Delta_{1z}(T_1, T_2, T_3), \quad (1)$$

where all terms in this expressions depend on the chemical potential μ_1 and μ_2 of the two graphene layers. Here $P_z^{(eq)}$ stands for the CLP at thermal equilibrium and is given by

$$P_z^{(eq)}(T) = \frac{k_B T}{\pi} \sum_{n=0}^{\infty} \int_0^{\infty} dQ Q \sum_p \left[\frac{e^{2qd}}{\tilde{\rho}_{1p} \tilde{\rho}_{2p}} - 1 \right]^{-1}, \quad (2)$$

where the prime on the sum means that the $n=0$ term is divided by 2, $q = [(\xi_n/c)^2 + Q^2]^{1/2}$ and $\xi_n = 2\pi n k_B T / \hbar$ are the Matsubara frequencies. $\tilde{\rho}_{1p}$ and $\tilde{\rho}_{2p}$ are the frequency-rotated reflection coefficients of bodies 1 and 2 respectively, p standing for either s (transverse electric TE) or p (transverse magnetic TM) polarization. The second term in the first equation corresponds to the nonequilibrium contribution, and is given by

$$\begin{aligned} \Delta_{1z}(T_1, T_2, T_3) = & A^{(ew)}(T_1) - A^{(ew)}(T_2) + B_1^{(pw)}(T_1) \\ & - B_1^{(pw)}(T_2) + B_2^{(pw)}(T_3) - B_2^{(pw)}(T_1) \\ & + B_3^{(pw)}(T_3) - B_3^{(pw)}(T_2), \end{aligned} \quad (3)$$

with

$$\begin{aligned} A^{(ew)}(T) &= \frac{\hbar}{2\pi^2} \sum_p \int_0^{\infty} d\omega \int_{\frac{\omega}{c}}^{\infty} dk k \operatorname{Im} k_z n(\omega, T) \frac{\operatorname{Im}(\rho_{1p} \rho_{2p}^*)}{|D_p|^2} e^{-2d \operatorname{Im} k_z}, \\ B_1^{(pw)}(T) &= -\frac{\hbar}{4\pi^2} \sum_p \int_0^{\infty} d\omega \int_0^{\frac{\omega}{c}} dk k k_z n(\omega, T) \frac{|\rho_{2p}|^2 - |\rho_{1p}|^2 + |\tau_{1p}|^2 (1 - |\rho_{2p}|^2)}{|D_p|^2}, \\ B_2^{(pw)}(T) &= -\frac{\hbar}{4\pi^2} \sum_p \int_0^{\infty} d\omega \int_0^{\frac{\omega}{c}} dk k k_z n(\omega, T) \left[\frac{|\tau_{1p}|^2 [1 + |\rho_{2p}|^2 (1 - |\tau_{1p}|^2)]}{|D_p|^2} - |\rho_{1p}|^2 - 2 \operatorname{Re} \left(\frac{\rho_{1p}^* \rho_{2p} \tau_{1p}^2}{D_p} e^{2ik_z(d+h_1)} \right) \right], \\ B_3^{(pw)}(T) &= -\frac{\hbar}{4\pi^2} \sum_p \int_0^{\infty} d\omega \int_0^{\frac{\omega}{c}} dk k k_z n(\omega, T) \left[\frac{|\tau_{2p}|^2}{|D_p|^2} (1 + |\rho_{1p}|^2 - |\tau_{1p}|^2) - 1 \right], \end{aligned} \quad (4)$$

where

$$D_p(\omega, \mu_1, T_1, \mu_2, T_2) = 1 - \rho_{1p} \rho_{2p} e^{2ik_z d}, \quad (5)$$

and

$$n(\omega, T) = \frac{1}{e^{\hbar\omega/k_B T} - 1}. \quad (6)$$

For TE polarization, and for the configuration described above, the Fresnel reflection and transmission coefficients are given by [24,27],

$$\begin{aligned} \rho_{j,s}(\omega, \mu_j, T_j) &= \frac{r_{a,j} + (1 + r_{a,j} + r_{b,j})r_{c,j} e^{2ik_z h_j}}{1 - r_{b,j} r_{c,j} e^{2ik_z h_j}}, \\ \tau_{j,s}(\omega, \mu_j, T_j) &= \frac{t_{a,j} t_{c,j} e^{i(k_z - k_z) h_j}}{1 - r_{b,j} r_{c,j} e^{2ik_z h_j}}, \end{aligned} \quad (7)$$

where

$$\begin{aligned} r_{a,j} &= \frac{k_z - \sigma_j \omega \mu_0 - k_{z,j}}{k_z + \sigma_j \omega \mu_0 + k_{z,j}}, \\ r_{b,j} &= \frac{k_{z,j} - \sigma_j \omega \mu_0 - k_z}{k_{z,j} + \sigma_j \omega \mu_0 + k_z}, \\ r_{c,j} &= \frac{k_{z,j} - k_z}{k_{z,j} + k_z}, \end{aligned} \quad (8)$$

and

$$\begin{aligned} t_{a,j} &= \frac{2k_z}{k_z + k_{z,j} + \mu_0 \omega \sigma_j}, \\ t_{c,j} &= \frac{2k_{z,j}}{k_z + k_{z,j}}. \end{aligned} \quad (9)$$

Here, $j = 1, 2$ denotes slab 1 or slab 2, $k_z = [(\omega/c)^2 - Q^2]^{1/2}$ and $k_{z,j} = [\varepsilon_j(\omega/c)^2 - Q^2]^{1/2}$ are the z components of the wave vectors for vacuum and for body j , respectively. σ_j is the graphene conductivity for each sheet and μ_0 is the permeability of vacuum.

For TM polarization, the Fresnel coefficients are given by [24,27]

$$\begin{aligned} \rho_{j,p} &= \frac{r_{d,j} + (1 - r_{d,j} - r_{e,j})r_{f,j}e^{2ik_{z,j}h_j}}{1 - r_{e,j}r_{f,j}e^{2ik_{z,j}h_j}}, \\ \tau_{j,p} &= \frac{t_{d,j}t_{f,j}e^{i(k_{z,j}-k_z)h_j}}{1 - r_{e,j}r_{f,j}e^{2ik_{z,j}h_j}}, \end{aligned} \quad (10)$$

where

$$\begin{aligned} r_{d,j} &= \frac{\varepsilon_j k_z - k_{z,j} + \frac{\sigma_j}{\omega \varepsilon_0} k_z k_{z,j}}{\varepsilon_j k_z + k_{z,j} + \frac{\sigma_j}{\omega \varepsilon_0} k_z k_{z,j}}, \\ r_{e,j} &= \frac{k_{z,j} - \varepsilon_j k_z + \frac{\sigma_j}{\omega \varepsilon_0} k_z k_{z,j}}{k_{z,j} + \varepsilon_j k_z + \frac{\sigma_j}{\omega \varepsilon_0} k_z k_{z,j}}, \\ r_{f,j} &= \frac{k_{z,j} - \varepsilon_j k_z}{k_{z,j} + \varepsilon_j k_z}, \end{aligned} \quad (11)$$

and

$$\begin{aligned} t_{d,j} &= \frac{2k_z \varepsilon_j}{k_{z,j} + k_z \varepsilon_j + k_z k_{z,j} \frac{\sigma_j}{\omega \varepsilon_0}}, \\ t_{f,j} &= \frac{2k_{z,j}}{k_z \varepsilon_j + k_{z,j}}, \end{aligned} \quad (12)$$

with ε_0 being the vacuum permittivity.

Finally, the reflection coefficients for imaginary frequencies can be obtained merely by setting $\omega = i\xi$, that is $\tilde{\rho}(\xi) = \rho(\omega = i\xi)$.

B. Graphene conductivity and dielectric function

The graphene conductivity $\sigma(\omega)$ [see Fig. 2 and Fig. 3] for real frequencies can be written as a sum of an interband and an intraband contributions, i.e., $\sigma = \sigma_{\text{inter}} + \sigma_{\text{intra}}$, respectively

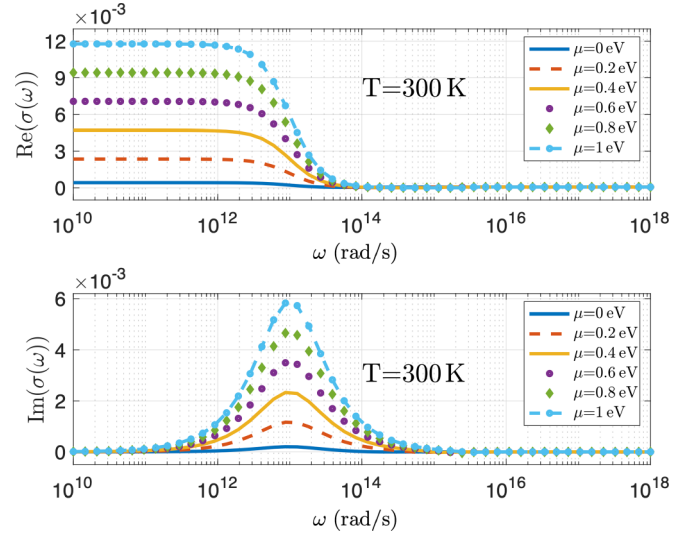


FIG. 2. Graphene conductivity (real and imaginary part) at real frequencies for several values of μ and at $T = 300$ K.

given by [28–30]:

$$\sigma_{\text{intra}}(\omega) = \frac{i8\sigma_0 k_B T}{\pi(\hbar\omega + i\hbar/\tau)} \ln \left[2 \cosh \left(\frac{\mu}{2k_B T} \right) \right], \quad (13)$$

$$\sigma_{\text{inter}}(\omega) = \sigma_0 \left[G \left(\frac{\hbar\omega}{2} \right) + i \frac{4\hbar\omega}{\pi} \int_0^{+\infty} \frac{G(x) - G(\frac{\hbar\omega}{2})}{(\hbar\omega)^2 - 4x^2} dx \right]. \quad (14)$$

Here, $\sigma_0 = e^2/4\hbar$ (expressed in Siemens), e is the electron charge, $G(x) = \sinh(x/k_B T)/[\cosh(\mu/k_B T) + \cosh(x/k_B T)]$, T is the graphene sheet temperature, τ is the relaxation time (we use $\tau = 10^{-13}$ s) and μ is the chemical potential. This model is accurate enough for the range of distances we study. In case of very short separations of very few nanometers more sophisticated models [31] can be used to obtain an even more precise estimation of the force. For Matsubara frequencies the

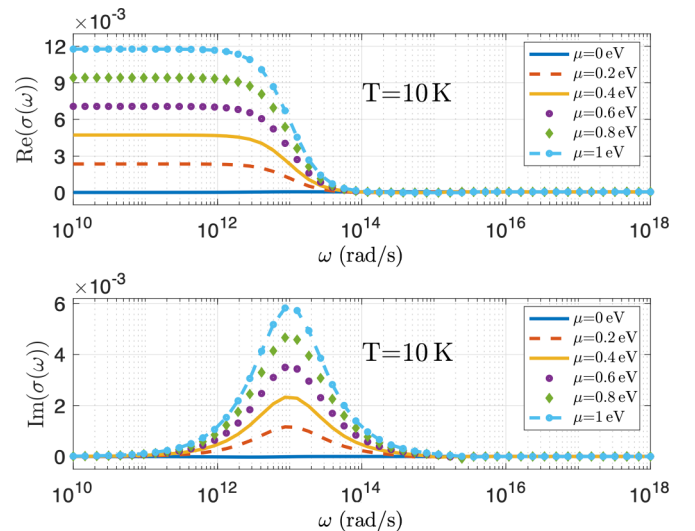


FIG. 3. Graphene conductivity (real and imaginary part) at real frequencies for several values of μ and at $T = 10$ K.

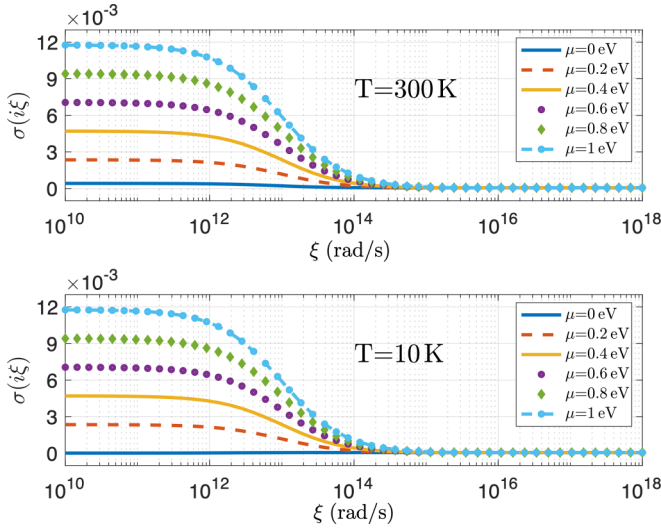


FIG. 4. Graphene conductivity at imaginary frequencies for several values of μ , at $T = 300$ K (upper panel) and $T = 10$ K (lower panel).

graphene conductivity (as shown in Fig. 4) can be expressed as the sum of its intraband and interband components [24]

$$\sigma_{\text{intra}}(i\xi_n) = \frac{8\sigma_0 k_B T}{\pi(\hbar\xi_n + \hbar/\tau)} \ln \left[2 \cosh \left(\frac{\mu}{2k_B T} \right) \right], \quad (15)$$

$$\sigma_{\text{inter}}(i\xi_n) = \frac{\sigma_0 4\hbar\xi_n}{\pi} \int_0^{+\infty} \frac{G(x)}{(\hbar\xi_n)^2 + 4x^2} dx. \quad (16)$$

Compared to the conductivity of graphene at $T = 300$ K and $\mu = 0$ eV [as shown in Fig. 5(a) for imaginary frequencies] or $T = 10$ K and $\mu = 0.2$ eV, the behavior of the conductivity at $T = 10$ K and $\mu = 0$ eV is different [as shown in Fig. 5(b)]. The same behavior can be seen for real frequencies [see Fig. 6(a) and Fig. 6(b)].

As already mentioned, we want to calculate the CLP out of thermal equilibrium between two parallel dielectric

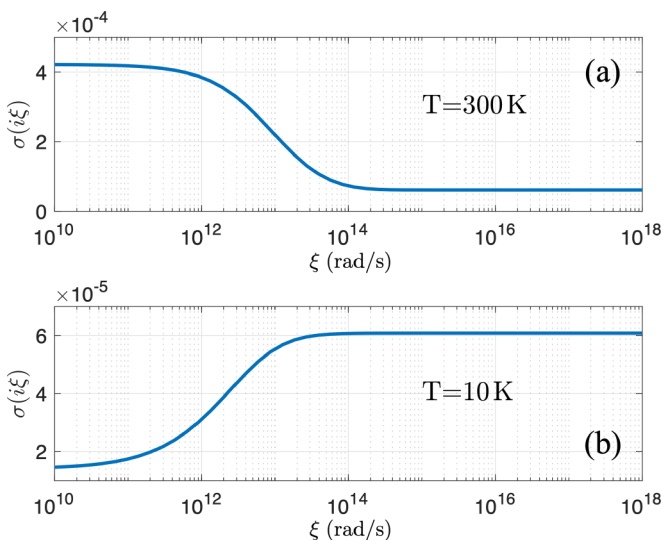


FIG. 5. Graphene conductivity at imaginary frequencies for $\mu = 0$ eV, at $T = 300$ K (upper panel) and $T = 10$ K (lower panel).

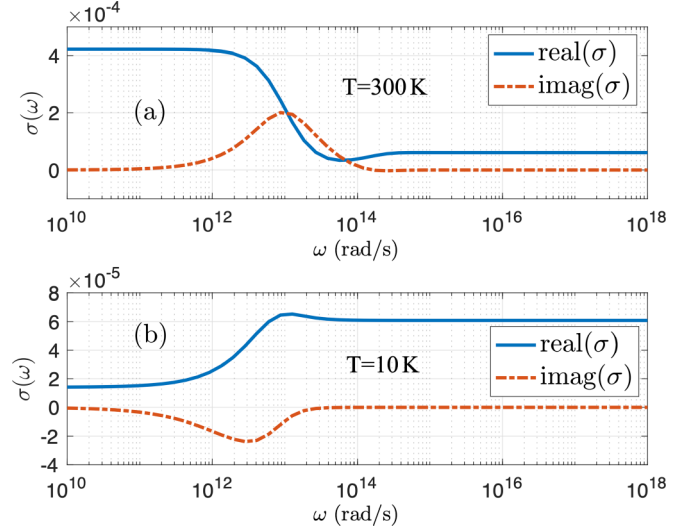


FIG. 6. Graphene conductivity at real frequencies for $\mu = 0$ eV, at $T = 300$ K (upper panel) and $T = 10$ K (lower panel).

slabs covered with a graphene sheets. For our study, we choose fused silica (SiO_2) with relative dielectric permittivity $\varepsilon(\omega) = \varepsilon'(\omega) + i\varepsilon''(\omega)$ taken from [32]. In Figs. 7(a) and 7(b) we show the real imaginary parts, respectively, of this dielectric function. For Matsubara frequencies, this function (which is necessarily real) can be deduced from the imaginary part $\varepsilon''(\omega)$ (for real frequencies) through the Kramers-Kronig relation given by the following equation [33,34]:

$$\varepsilon(i\xi) = 1 + \frac{2}{\pi} \int_0^{\infty} \frac{\omega \varepsilon''(\omega)}{\omega^2 + \xi^2} d\omega, \quad (17)$$

represented in Fig. 7(c).

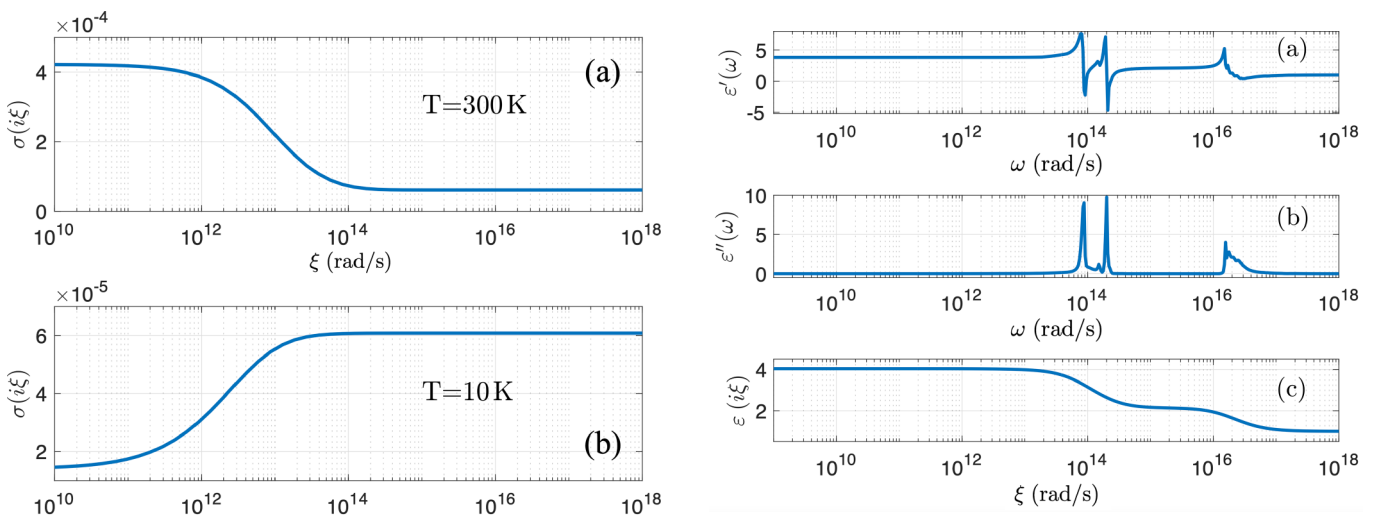


FIG. 7. Relative dielectric permittivity of fused silica (SiO_2). (a) Real and (b) imaginary parts of $\varepsilon(\omega)$ on the real frequency axis, and (c) permittivity $\varepsilon(i\xi)$ on the imaginary frequency axis.

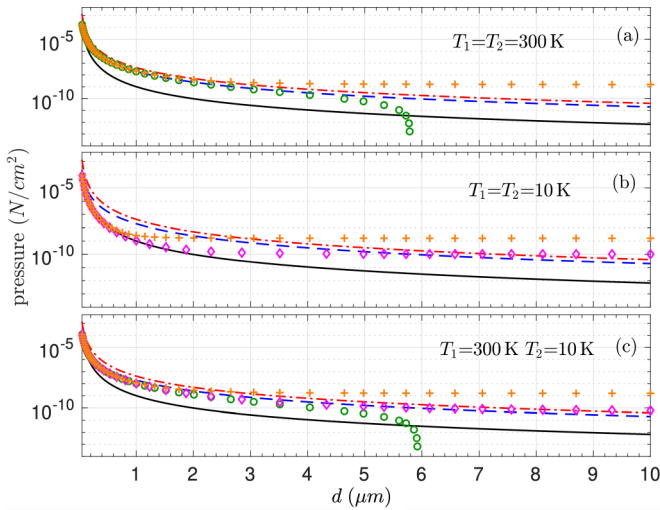


FIG. 8. Comparison of the CLP out of thermal equilibrium [Eq. (1)] and in thermal equilibrium [Eq. (2)] acting on body 1, between two graphene sheets with chemical potentials $\mu_1 = \mu_2 = 0$ eV. Lines show equilibrium pressures at $T = 10$ K (black solid), 300 K (blue dashed), and 600 K (red dash-dotted). Symbols show nonequilibrium pressures at $T_3 = 10$ K (green circles), 300 K (magenta diamonds), and 600 K (orange plus). $T_1 = T_2 = 300$ K in panel (a), $T_1 = T_2 = 10$ K in panel (b), and $T_1 = 300$ K and $T_2 = 10$ K in panel (c).

III. RESULTS

A. Out of thermal equilibrium effect

In the previous section, we presented the theory behind the CLP out of thermal equilibrium and its dependence on temperature, the chemical potential of the graphene sheet, and also the distance between objects. In this section, we discuss the specific results obtained for the CLP between two graphene sheets ($\mu_1 = \mu_2 = 0$ eV) without a substrate. The results are shown in Fig. 8, which displays the CLP as a function of distance for various configurations (see caption of Fig. 8 for details).

The green circles in Fig. 8(a) show that when the two graphene sheets are at the same temperature $T_1 = T_2 = 300$ K, and the environment is at $T_3 = 10$ K, the CLP is attractive at small d , causing them to be pushed towards each other. However, as the distance increases, the force decreases and eventually becomes repulsive at distances greater than $5.8 \mu\text{m}$. To better show this sign change, the pressure is displayed on a linear scale (between 5 and $10 \mu\text{m}$) in Fig. 9(a).

Considering a scenario where the first graphene sheet is at $T_1 = 300$ K and the second at $T_2 = 10$ K, the sign change in pressure occurs at a slightly larger separation distance of around $6 \mu\text{m}$ [see Fig. 9(b) with linear scale] compared with the previous case where $T_1 = T_2 = 300$ K. Figure 8(a) plots the CLP for the case when the environment is at $T_3 = 600$ K and the sheets are at the same temperature $T_1 = T_2 = 300$ K. As the CLP decreases with the separation distance, it becomes greater than the pressure at any thermal equilibrium (10, 300, and 600 K) for large separation distances (from around $3 \mu\text{m}$). This behavior is also observed if we cool down one of the sheets [$T_1 = 300$ K and $T_2 = 10$ K, see Fig. 8(c)] or both of

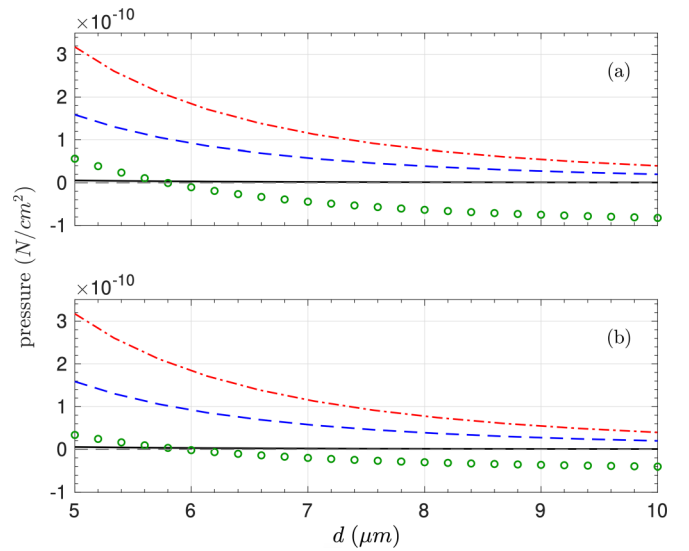


FIG. 9. Zoom of Fig. 8 on linear scales, using the same conventions. The change in sign of the force is clearly visible.

them [$T_1 = T_2 = 10$ K, see Fig. 8(b)]. Such behavior is in contrast to the equilibrium case where the CLP decreases when the system is cooled down. It is worth noticing that the distance at which OTE-CLP becomes predominant is shifted by an amount that depends on the temperatures of the graphene sheets. For the system parameters we considered, this behavior appears to be a general trend happening whenever departing from an equilibrium situation and cooling down the sheets (while preserving the temperature of the environment).

Next, we extend our study to the case where two graphene sheets are placed on fused silica slabs with finite thicknesses $h_1 = h_2 = 2 \mu\text{m}$. The CLP is calculated and compared with the previous case of two graphene sheets without substrates. Our results, shown in Fig. 10, indicate that the behavior of the CLP shows similar features compared with the previous case. The attractive force is dominant at short distances and eventually becomes repulsive at larger distances when the environment is at $T_3 = 10$ K. However, we observe that the presence of the substrate slightly modifies the distance where the sign changes (As illustrated in Fig. 11, which is plotted on a linear scale). Overall, the results suggest that the presence of the fused silica substrate does not lead to qualitatively new features for on the CLP between the graphene sheets.

B. Chemical potential effect

1. Thermal equilibrium

To begin, let us examine the chemical potential effect on the CLP at thermal equilibrium. To study the relative variation of the pressure as function of the chemical potential (assuming that $\mu_1 = \mu_2$) we define the function

$$\Delta P_\mu = \frac{P_{1z}(\mu) - P_{1z}(\mu = 0)}{P_{1z}(\mu = 0)}, \quad (18)$$

where P_{1z} is given by Eq. (2) or Eq. (1), for configurations at or out of thermal equilibrium, respectively.

Figure 12 displays the relative variation ΔP_μ for different values of the chemical potential with respect to the situation

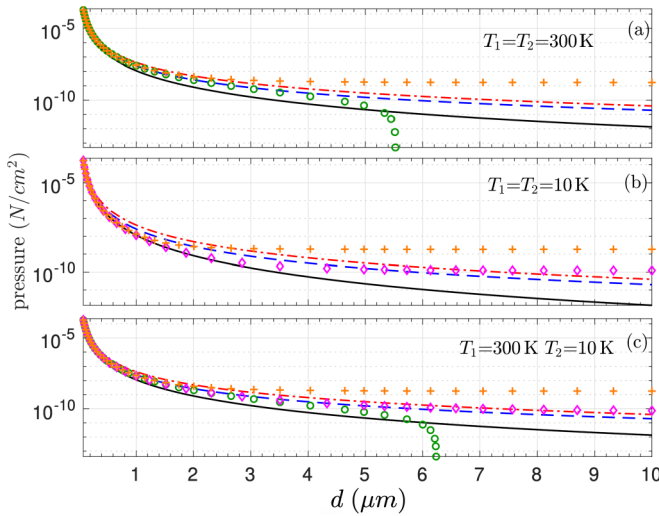


FIG. 10. Comparison of the CLP out of thermal equilibrium [Eq. (1)] and in thermal equilibrium [Eq. (2)] acting on body 1, between two fused silica slabs ($h_1 = h_2 = 2 \mu\text{m}$) covered with graphene sheets (chemical potential $\mu_1 = \mu_2 = 0 \text{ eV}$). Lines show equilibrium pressures at $T = 10 \text{ K}$ (black solid), 300 K (blue dashed), and 600 K (red dash-dotted). Symbols show nonequilibrium pressures at $T_3 = 10 \text{ K}$ (green circles), 300 K (magenta diamonds), and 600 K (orange plus). $T_1 = T_2 = 300 \text{ K}$ in panel (a), $T_1 = T_2 = 10 \text{ K}$ in panel (b), and $T_1 = 300 \text{ K}$ and $T_2 = 10 \text{ K}$ in panel (c).

where $\mu = 0 \text{ eV}$. This is done for two different configurations: suspended graphene sheets [Figs. 12(a)–12(c)] and slabs of SiO_2 covered with graphene sheets [Figs. 12(d)–12(f)].

Focusing on Fig. 12(a), which represents the $T = 10 \text{ K}$ case, it is evident that as the chemical potential increases, there is a simultaneous increase in the pressure. The graph exhibits a bell-shaped curve, with the relative variation being minimal at both small and large distances (universal graphene-graphene interaction and the thermal limits [35,36]), and reaching

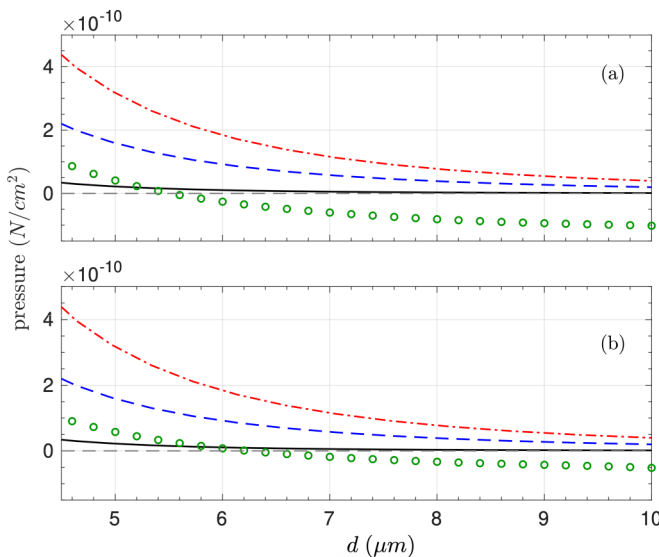


FIG. 11. Zoom of Fig. 9 on linear scales, using the same conventions. The change in sign of the force is clearly visible.

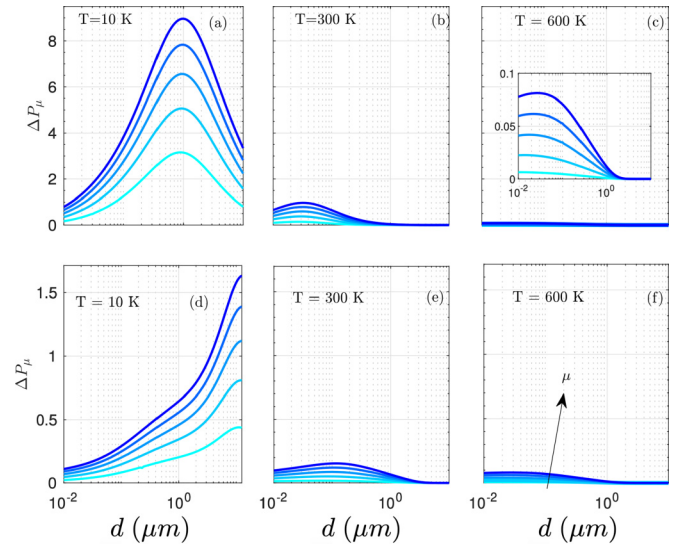


FIG. 12. Relative variation ΔP_μ of the CLP at thermal equilibrium as a function of (a)–(c) the distance between the two suspended graphene sheets and (d)–(f) covered slabs of SiO_2 . We plot ΔP_μ for $\mu = 0.2, 0.4, 0.6, 0.8, 1 \text{ eV}$.

its maximum at $1 \mu\text{m}$. Furthermore, when the temperature increases, the effect of the chemical potential diminishes significantly and the maximum of ΔP_μ shifts towards smaller distances. For instance, at $T = 300 \text{ K}$ [Fig. 12(b)], the maximum variation occurs around 30 nm . This effect is due to the change in the thermal wavelength λ_T which depends on the temperature. For the same reason, when the temperature is increased to $T = 600 \text{ K}$ [Fig. 12(c)], ΔP_μ becomes even smaller, and its maximum shifts to around 10 nm .

We then proceed to the second case involving two slabs of SiO_2 covered with graphene sheets. When $T = 10 \text{ K}$ [Fig. 12(d)], it can be observed that, compared with the case of two graphene sheets without a substrate, the maximum shifts to the right, because the CLP is dominated in this case by the μ -independent substrate (for distances smaller than $8 \mu\text{m}$), and the variation decreases. Furthermore, as the temperature increases, such as at $T = 300 \text{ K}$ [Fig. 12(e)] and $T = 600 \text{ K}$ [Fig. 12(f)], the maximum shifts towards the left, and the chemical potential effect decreases.

2. Out of thermal equilibrium: Suspended graphene sheets

Besides examining the influence of nonequilibrium conditions on the CLP, we also explored how the chemical potential affects this pressure. Let us start considering the two graphene sheets being at the same chemical potential $\mu = \mu_1 = \mu_2$. Figure 13 shows ΔP_μ between two graphene sheets for different values of the chemical potential ($0.2, 0.4, 0.6, 0.8, 1 \text{ eV}$). Our results reveal that when $T_1 = T_2 = 300 \text{ K}$, varying the environment temperature T_3 does not lead to significant changes of the CLP for all μ , as shown in Figs. 13(a) and 13(b). This situation is comparable to the thermal equilibrium case as shown in Fig. 12(a). In both Figs. 13(a) and 13(b), as the chemical potential increases, the relative variation of the nonequilibrium pressure also increases, reaching approximately a value of 1 when $\mu = 1 \text{ eV}$ and the separation distance is near 30 nm . On the other hand, when $T_1 = T_2 =$

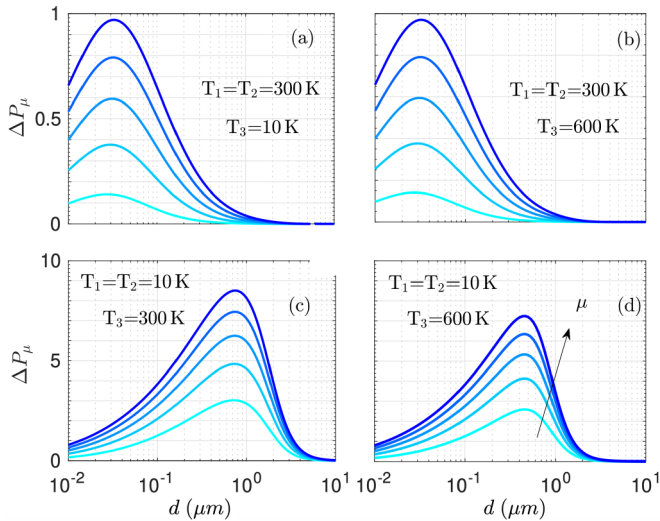


FIG. 13. Relative variation ΔP_μ of the CLP as a function of the distance between the two suspended graphenes with $T_1 = T_2$.

10 K and $T_3 = 300$ K, as shown in Fig. 13(c), the impact of the chemical potential becomes much stronger. Specifically, when the separation distance is around 500 nm, the CLP with $\mu = 1$ eV becomes about 10 times greater than when $\mu = 0$ eV and d is near 500 nm. The relative variation is further demonstrated in Fig. 13(d) when the environment temperature is increased to 600 K, where the effect is slightly lower than in the previous case. Our findings suggest that the chemical potential has a substantial impact only when the graphene sheets are at low temperatures.

To further understand the impact of the chemical potential on the CLP between two graphene sheets, we extend our investigation to the case where the two sheets are at different temperatures. As shown in Fig. 14(a), where $T_1 = 300$ K, $T_2 = 10$ K, and $T_3 = 10$ K, the relative variation increases with chemical potential, and the pressure for $\mu = 1$ eV is larger than that for $\mu = 0$ eV before the sign change.

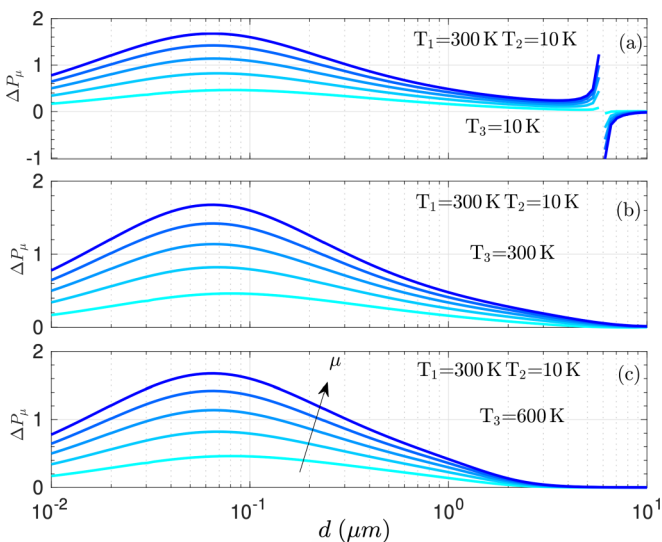


FIG. 14. Relative variation ΔP_μ of the CLP as a function of the distance between the two suspended graphenes with $T_1 \neq T_2$.

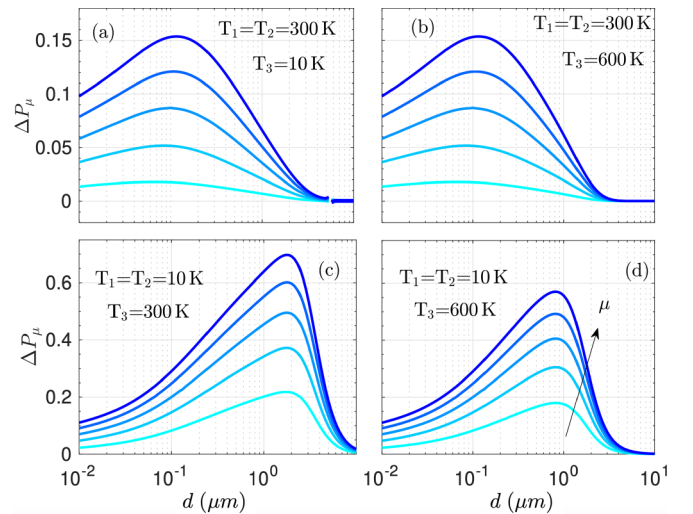


FIG. 15. Relative variation ΔP_μ of the CLP as a function of the distance between two slabs of SiO_2 covered with graphene sheets with $T_1 = T_2$.

However, beyond a separation distance of 6 μm (where the pressure becomes repulsive) the CLP becomes smaller when $\mu = 1$ eV than when $\mu = 0$ eV. Furthermore, it is worth noticing that the singularities in Fig. 14(a) are due to the fact that we are dividing by the pressure at $\mu = 0$ eV, which is very low. We notice also that the relative variation of the pressure increases with the chemical potential, and is the most important when $\mu = 1$ eV and $d = 60$ nm, except for the case where $T_3 = 10$ K and $d > 6$ μm .

3. Out of thermal equilibrium: Fused silica slabs covered with graphene sheets

In the previous section, we examined the impact of the chemical potential on the (CLP) between two graphene sheets under nonequilibrium conditions. We now turn our attention to a system composed of two graphene sheets covering two fused silica substrates with identical thicknesses of $h_1 = h_2 = 2$ μm .

Our results, shown in Figs. 15(a) and 15(b), reveal that the relative variation of the pressure in this system is significantly smaller than in the previous case, reaching a maximum value of only 0.15 when both objects are at 300 K regardless of T_3 . Furthermore, this maximum is shifted slightly to the right, towards a separation distance of 100 nm (30 nm in the case of suspended graphene).

It should be noted that, when the two graphene sheets are at 300 K and the environment temperature is 10 K, the effect of the chemical potential after the change in sign, i.e., after 6 μm , is very small.

On the other hand, as the temperature of the graphene sheets decreases to $T_1 = T_2 = 10$ K, the relative variation increases, with a maximum value of 0.75 for $T_3 = 300$ K, as shown in Fig. 15(c). In this case, we observe that the maximum occurs at a larger separation distance, between 1 and 2 μm , and shifts towards greater distances.

Notably, for $T_3 = 600$ K, the maximum relative variation occurs between 900 nm and 1 μm , as shown in Fig. 15(d),

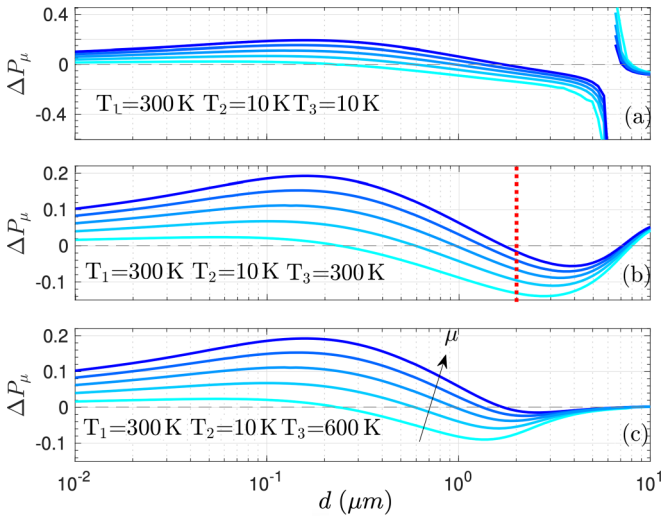


FIG. 16. Relative variation ΔP_μ of the CLP as a function of the distance between two slab of SiO_2 covered with graphene sheets with $T_1 \neq T_2$.

which is smaller than the previous case. Nevertheless, the maximum value is still significant, and the overall trend remains similar to the case of $T_3 = 300$ K.

We consider now the case where the two objects are at different temperatures, $T_1 \neq T_2$. Figure 16(a) displays ΔP_μ for different temperatures T_3 of the environment. First of all, let us recall that the CLP increases with the chemical potential for suspended graphene sheets if the pressure is attractive. We retrieve this behavior in Figs. 16 for distances less than a certain value depending on μ . For example, this distance is about $1.72 \mu\text{m}$ for $\mu = 1$ eV regardless of T_3 . This behavior is shown in Fig. 17, where we directly display the CLP for $\mu = 0$ eV and $\mu = 1$ eV with a zoom around their first intersection [see Fig. 17(a)].

In the specific case where T_3 is fixed at 10 K, we observe that at distances larger than $1.7 \mu\text{m}$, the pressure for $\mu = 1$ eV

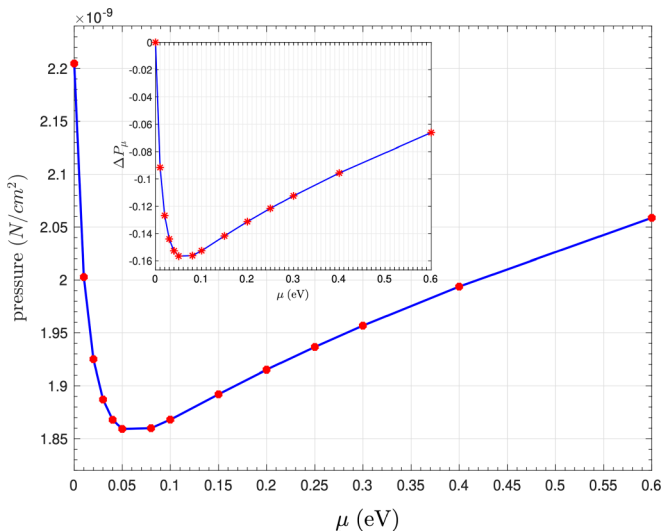


FIG. 17. CLP out of thermal equilibrium [Eq. (1)] between two slabs of SiO_2 covered with graphene sheets. $T_1 = 300$ K, $T_2 = 10$ K, and $T_3 = 300$ K and for $\mu = 0$ eV and $\mu = 1$ eV.

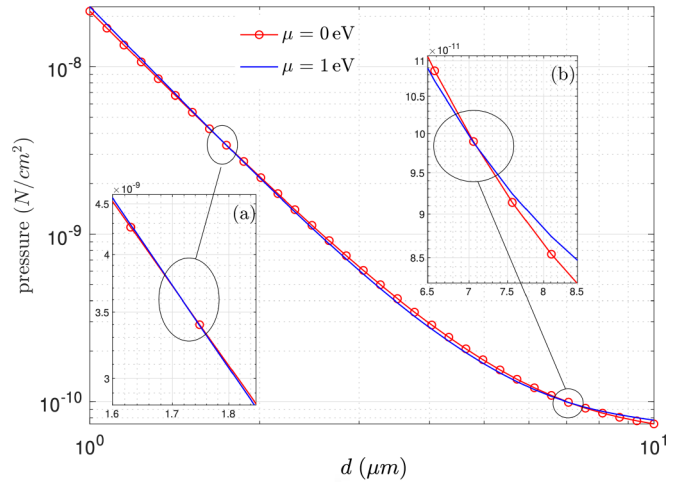


FIG. 18. CLP out of thermal equilibrium [Eq. (1)] between two slabs of SiO_2 covered with graphene sheets separated by $d = 2 \mu\text{m}$ and $T_1 = 300$ K, $T_2 = 10$ K, and $T_3 = 300$ K.

is lower than that for $\mu = 0$ eV until a change in sign occurs at around $6 \mu\text{m}$. Subsequently, the pressure for $\mu = 1$ eV becomes greater than that for $\mu = 0$ eV again (when $d < 7 \mu\text{m}$). Beyond this distance, the pressure for $\mu = 1$ eV once again becomes lower than that for $\mu = 0$ eV.

We now shift our attention to the case at $T_3 = 300$ K [see Fig. 16(b)]. It is noteworthy that between 1.7 and $7 \mu\text{m}$, as the chemical potential decreases, the relative variation is expected to approach zero. However, this is not what we observe because the smallest value of μ we are considering is only 0.2 eV. To clarify this point, we focus on a specific distance of $2 \mu\text{m}$ [red dotted line in Fig. 16(b)] and gradually decrease the chemical potential towards zero, as shown in Fig. 18 where we display the CLP for different values of μ and also ΔP_μ in the inset. It becomes apparent that this variation is not monotonic. The nonmonotonic dependence of the CLP represents a novel feature of nonequilibrium systems that is absent in their equilibrium counterparts. This variation eventually tends towards zero for small values of the chemical potential (below 0.1 eV). After $7 \mu\text{m}$, the opposite occurs, ΔP_μ becomes monotonic, and this is clearly shown in Fig. 17(b).

Finally, for the case of $T_3 = 600$ K, we observe the same behavior as in the previous cases, with the pressure for $\mu = 1$ eV being lower than that for $\mu = 0$ eV after $1.7 \mu\text{m}$. However, as the distance increases, the relative variation tends towards zero, indicating that the difference in CLP between the chemical potentials becomes negligible at larger separations. This behavior is illustrated in Fig. 16(c).

When the CLP becomes repulsive, it decreases with chemical potential on the contrary of what happens when it is attractive. This can be directly seen in Fig. 16(a) for $d > 6.2 \mu\text{m}$.

IV. CONCLUSIONS

We studied the OTE CLP between two graphene layers at two different temperatures in a thermal bath of a third temperature. The graphene layers can be suspended or coated on a fused silica substrate. Unlike the equilibrium case where

the pressure is always attractive, the pressure can be tuned to change sign and become repulsive. The repulsive interactions could play a role in alleviating stiction in graphene nanomechanical systems. We also show that the CLP on graphene can be tuned by the chemical potentials. To obtain large changes of the CLP, we find that the temperatures of the graphene sheets need to be kept low in both equilibrium and nonequilibrium situations. While the CLP at equilibrium increases with chemical potential for all distances and temperatures we considered, we find that for OTE CLP the dependence on the chemical potential becomes nonmonotonic at certain ranges of distance. Finally, one interesting addi-

tional degree of liberty that can bring new effect is anisotropy. This is present, e.g., in black phosphorus which has been used to explore the Casimir interaction at thermal equilibrium [37].

ACKNOWLEDGMENTS

The work described in this paper was partially supported by a grant “CAT,” No. A-HKUST604/20, from the ANR/RGC Joint Research Scheme sponsored by the French National Research Agency (ANR) and the Research Grants Council (RGC) of the Hong Kong Special Administrative Region. We acknowledge P. Rodriguez-Lopez for useful discussions.

-
- [1] E. M. Lifshitz, *J. Exper. Theoret. Phys. USSR* **29**, 94 (1955) [*Sov. Phys.* **2**, 73 (1956)].
- [2] I. Dzyaloshinskii, E. Lifshitz, and L. Pitaevskii, *Adv. Phys.* **10**, 165 (1961).
- [3] H. B. G. Casimir, *Indag. Math.* **10**, 261 (1948).
- [4] M. Antezza, Ph.D. thesis, University of Trento, Italy (2006).
- [5] M. Antezza, L. P. Pitaevskii, and S. Stringari, *Phys. Rev. Lett.* **95**, 113202 (2005).
- [6] M. Antezza, *J. Phys. A: Math. Gen.* **39**, 6117 (2006).
- [7] M. Antezza, L. P. Pitaevskii, S. Stringari, and V. B. Svetovoy, *Phys. Rev. Lett.* **97**, 223203 (2006).
- [8] J. M. Obrecht, R. J. Wild, M. Antezza, L. P. Pitaevskii, S. Stringari, and E. A. Cornell, *Phys. Rev. Lett.* **98**, 063201 (2007).
- [9] M. Antezza, L. P. Pitaevskii, and S. Stringari, *Phys. Rev. A* **70**, 053619 (2004).
- [10] S. Y. Buhmann and S. Scheel, *Phys. Rev. Lett.* **100**, 253201 (2008).
- [11] Y. Sherkunov, *Phys. Rev. A* **79**, 032101 (2009).
- [12] M. Antezza, L. P. Pitaevskii, S. Stringari, and V. B. Svetovoy, *Phys. Rev. A* **77**, 022901 (2008).
- [13] G. Bimonte, *Phys. Rev. A* **80**, 042102 (2009).
- [14] R. Messina and M. Antezza, *Phys. Rev. A* **84**, 042102 (2011).
- [15] R. Messina and M. Antezza, *Europhys. Lett.* **95**, 61002 (2011).
- [16] R. Messina and M. Antezza, *Phys. Rev. A* **89**, 052104 (2014).
- [17] D. Polder and M. Van Hove, *Phys. Rev. B* **4**, 3303 (1971).
- [18] M. Krüger, T. Emig, and M. Kardar, *Phys. Rev. Lett.* **106**, 210404 (2011).
- [19] M. Krüger, G. Bimonte, T. Emig, and M. Kardar, *Phys. Rev. B* **86**, 115423 (2012).
- [20] A. Noto, R. Messina, B. Guizal, and M. Antezza, *Phys. Rev. A* **90**, 022120 (2014).
- [21] V. Svetovoy, Z. Moktadir, M. Elwenspoek, and H. Mizuta, *Europhys. Lett.* **96**, 14006 (2011).
- [22] A. A. Banishev, H. Wen, J. Xu, R. K. Kawakami, G. L. Klimchitskaya, V. M. Mostepanenko, and U. Mohideen, *Phys. Rev. B* **87**, 205433 (2013).
- [23] G. Gómez-Santos, *Phys. Rev. B* **80**, 245424 (2009).
- [24] C. Abbas, B. Guizal, and M. Antezza, *Phys. Rev. Lett.* **118**, 126101 (2017).
- [25] M. Liu, Y. Zhang, G. L. Klimchitskaya, V. M. Mostepanenko, and U. Mohideen, *Phys. Rev. Lett.* **126**, 206802 (2021).
- [26] G. L. Klimchitskaya, V. M. Mostepanenko, and O. Y. Tsybin, *Phys. Rev. B* **105**, 195430 (2022).
- [27] B. Zhao, B. Guizal, Z. M. Zhang, S. Fan, and M. Antezza, *Phys. Rev. B* **95**, 245437 (2017).
- [28] L. A. Falkovsky, *J. Phys.: Conf. Ser.* **129**, 012004 (2008).
- [29] L. A. Falkovsky and A. A. Varlamov, *Eur. Phys. J. B* **56**, 281 (2007).
- [30] S. A. Awan, A. Lombardo, A. Colli, G. Privitera, T. S. Kulmala, J. M. Kivioja, M. Koshino, and A. C. Ferrari, *2D Mater.* **3**, 015010 (2016).
- [31] A. H. Castro Neto, F. Guinea, N. M. R. Peres, K. S. Novoselov, and A. K. Geim, *Rev. Mod. Phys.* **81**, 109 (2009).
- [32] W. J. Tropf and M. E. Thomas, *Handbook of Optical Constants of Solids*, edited by E. Palik (Academic Press, Inc., New York, 1998).
- [33] R. de L. Kronig, *J. Opt. Soc. Am.* **12**, 547 (1926).
- [34] L. D. Landau and E. Lifshitz, *Electrodynamics of Continuous Media* (Pergamon Press, Oxford, 1960).
- [35] P. Rodriguez-Lopez, W. J. Kort-Kamp, D. A. Dalvit, and L. M. Woods, *Nat. Commun.* **8**, 14699 (2017).
- [36] L. M. Woods, D. A. R. Dalvit, A. Tkatchenko, P. Rodriguez-Lopez, A. W. Rodriguez, and R. Podgornik, *Rev. Mod. Phys.* **88**, 045003 (2016).
- [37] L. Wang, H. Sun, Y. Jia, L. Ge, Z. Ji, and K. Gong, *Opt. Express* **31**, 15204 (2023).

Correction: Equations (4), (7), (9), and (10) contained errors and have been fixed.